Mechanical design of a nested 4-layer Canted Cosine Theta (CCT) dipole

Rafal Ortwein[1], Jacek Blocki[1], Glyn Kirby[2] and Jeroen van Nugteren[2]

[1]Division of Scientific Equipment and Infrastructure Construction, Institute of Nuclear Physics of the Polish Academy of Sciences, ul. Radzikowskiego 152, 31-342 Cracow, Poland
[2]Technology Department, European Organization for Nuclear Research CERN, 1211 Geneva 23, Switzerland

rafal.ortwein@ifj.edu.pl

Abstract. Nested CCT dipoles could be used in particle accelerators and proton therapy machines to bend a beam of charged particles in any direction. In the present study, a mechanical design of a 4 layer nested CCT dipole is evaluated with Finite Element Method (FEM). A full parametric 3D model of a 2.5 Tm 4-layer CCT dipole has been developed using the APDL scripting in the ANSYS software. The, so called, bottom up approach with direct generation of nodes and elements has been utilized, optimizing for the speed of the model generation as the time consuming meshing was bypassed. The properties of the Nb-Ti strands with the surrounding CTD-101K epoxy were obtained with a dedicated homogenization model. Resulting orthotropic properties were fully accounted for in the simulation. The shear stresses in the bonding composite layer: Kapton+S2-glass+CTD-101K were computed. With the results above the limit of 10 MPa, the necessity to provide additional rigidity against the torque was confirmed – castellated design. The shear stresses were mostly caused by thermal effects, and only ~25 % was caused by the Lorentz forces. The influence of the boundary conditions was analysed, leading to their optimal choice limiting the deformation due to Lorentz forces to 91 μm.

1. Introduction

The CCT magnets (originally named skewed solenoids [1]) are being strongly developed as offering many potential advantages over the cosine-theta, one of the most important being the lower stresses in the superconducting coils due to the support of each individual turn [2]. CCT magnets have flexibility of producing any multipole field, via control of the cable path. Up to now, 2 prototypes of CCT magnets wound with Rutherford Nb-Ti cables were build and tested [3] as well as three CCT dipole prototypes with Nb3Sn Rutherford cables [4]. The MCBRB (2.65 T bore field, 5 Tm integrated field) orbit correctors for the recombination dipole D2 for the High Luminosity upgrade of the Large Hadron Collider - HL-LHC [5] are made in CCT technology [6-7]. The development of the CCT dipoles for the HL-LHC brought the idea of nested CCT dipoles, with possible applications in particle accelerators (e.g. orbit correctors) and proton therapy machines [8]. Nested dipoles allow control of the magnetic field vector in the full range 0-360º. Currently, the PSI Institute is developing CCT technology with the goal of advancing the technology for 16 T magnets to satisfy the FCC requirements [9-10]. Recently a study showed validity of building CCT magnets from REBCO CORC® HTS wires [11].

Several works have been devoted to 3D periodic FEM models of CCT magnets [12-16]. Whereas only one paper was devoted to the full 3D model of a CCT magnet [17]. In that work the experimental

results from the strain gauges placed on the CCT4 prototype have been compared to the 3D simulations with good agreement.

In the present paper, a parametric 3D model of the nested CCT dipole is presented. The model was implemented in the APDL script in the ANSYS software to provide a full parametrization to the magnet's geometry. In addition, the meshing was bypassed via direct generation of nodes and element to maximally speed-up the pre-processing phase. This work is the direct development of the previous work [18] which was focused on developing a 3D periodic model and 2D models capable of modeling the nested CCT dipoles. Two types of boundary conditions were considered in this study according to the 1st and the 2nd design iterations. The interlayer composite was modeled according to the 1st design, having thickness of 0.3 mm The results of the simulations allowed concluding on the final design choice of the castellated design for the engineering solution of the nested CCT dipole.

2. Geometry of a 3D CCT layer

The framework of describing geometry of a CCT layer was introduced in [18]. In the simplest case capable of modelling all the necessary components of the nested CCT dipole magnet, each of the layer contains 3 sub-layers: the coil, the spar (bottom part of the former) and the interlayer insulation. For such a geometry (Figure 1) the parametric equations describing position of the corners (positions of nodes) in cylindrical coordinate system are [18]:

$$\vec{r}_{ji}(\theta) = (R_{Ci} + X_{rji})\hat{r} + \frac{X_{bji}C(\theta)}{D(\theta)}\hat{\theta} + \left(\frac{R_{Ci}\sin(\theta-\theta_{0i})}{\mathrm{tg}(\alpha_i)} + \frac{w_i(\theta-\theta_{0i})}{2\pi} + z_{0i} - \frac{X_{bji}R_{Ci}}{D(\theta)}\right)\hat{z} \quad (1)$$

$$C(\theta) = R_{Ci}\cot(\alpha_i)\cos(\theta-\theta_{0i}) + \frac{w_i}{2\pi} \quad (2)$$

$$D(\theta) = \left[R_{Ci}^2 + \left(R_{Ci}\cot(\alpha_i)\cos(\theta-\theta_{0i}) + \frac{w_i}{2\pi}\right)^2\right]^{1/2} = \left[R_{Ci}^2 + C(\theta)^2\right]^{1/2} \quad (3)$$

where j={A, B, D, E, F, G, H, I, J, K, L, M, O, P}, i - layer number, R_{Ci} – is the radius of the CCT axis (passing through the geometric center of the coil) of the i-th layer, θ is the angle in the xy plane of the center C, X_{rji} – is the distance from the j point from the center C along the r-axis, X_{bji} – is the distance of the point j from the center C along the b-axis, α_i – is approximately the tilt angle of i-th layer, θ_{0i} – is the angle corresponding to the beginning of the i-th layer, w_i – is the pitch of i-th layer, z_{0i} – is the z-coordinate corresponding to the beginning of a turn in the i-th layer

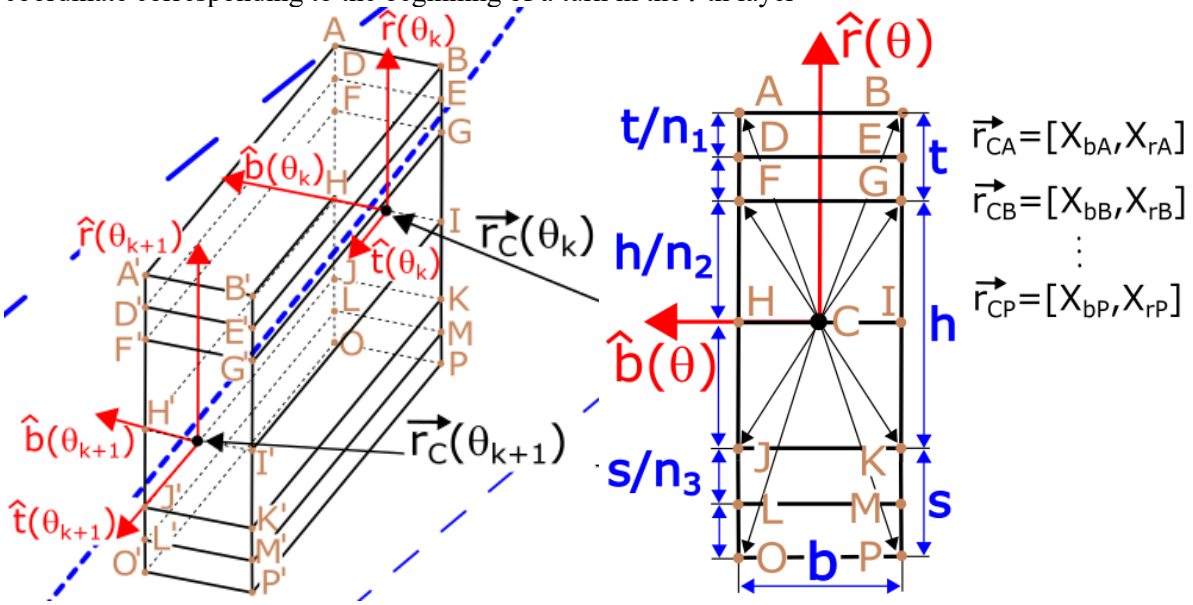

Figure 1. a) Two consecutive cross-sections of a CCT layer; b) dimensions of the cross-section in the local coordinate system *Crb*.

After inserting the formulas for the unit vectors in cylindrical coordinate system $\hat{r} = \hat{\imath}\cos(\theta) + \hat{\jmath}\sin(\theta)$, $\hat{\theta} = -\hat{\imath}\sin(\theta) + \hat{\jmath}\cos(\theta)$, $\hat{z} = \hat{k}$ into Equation 1 one obtains Cartesian equivalent:

$$\vec{r}_{ji}(\theta) = \hat{\imath}\left[\left(R_{\mathrm{C}i} + X_{\mathrm{r}ji}\right)\cos(\theta) - \frac{X_{\mathrm{b}ji}C(\theta)}{D(\theta)}\sin(\theta)\right] + \hat{\jmath}\left[\left(R_{\mathrm{C}i} + X_{\mathrm{r}ji}\right)\sin(\theta) + \frac{X_{\mathrm{b}ji}C(\theta)}{D(\theta)}\cos(\theta)\right] + \hat{k}\left[\frac{R_{\mathrm{C}i}\sin(\theta - \theta_{0i})}{\mathrm{tg}(\alpha_i)} + \frac{w_i(\theta - \theta_{0i})}{2\pi} + z_{0i} - \frac{X_{\mathrm{b}ji}R_{\mathrm{C}i}}{D(\theta)}\right] \quad (4)$$

The geometrical parameters of the four layer nested CCT dipole magnet are listed in Table 1.

Table 1. Parameters of the 4-layer nested CCT dipole [18]

Parameter		Layer 1	Layer 2	Layer 3	Layer 4
b, h, L	[mm]		2, 5, 1400		
R_z	[mm]	84	93.3	102.6	111.9
t (interlayer th.)	[mm]	0.3	0.3	0.3	0.3
$R_{zr}=R_z+t$	[mm]	84.3	93.6	102.9	112.2
R_w	[mm]	75	84.3	93.6	102.9
$R_{Ci}=(R_z - h/2)$	[mm]	81.5	90.8	100.1	109.4
w_i	[mm]	4.854	4.854	4.5295	4.5295
α_i	[^{0}]	-31.79375	31.71078	-34.17021	34.11232
θ_{0i}	[^{0}]	180	180	270	270
z_{0i}	[mm]	-550.930	-550.930	-536.746	-536.746
n_{turn}	[-]	227	227	237	237
Outer cylinder	[mm]		R_{w_cyl}=112.2, R_{z_cyl}=132.9		

In order to have a control over the mesh in the radial direction each of the 3 sub-layers (Figure 1) was further divided, with $n_1$divisions for the interlayer, n_2 for the coil and n_3 for the bottom part of the former. Requiring describing the positions of n_P points (Figure 1b):

$$n_P = 2 \cdot (n_1 + n_2 + n_3 + 1) \quad (5)$$

The geometry created directly from the Equation 1 would make the elements between the turns significantly skewed (Figure 2a). In order to introduce more regular mesh into the 3D model, it was beneficial to create it in such a way that all the points (Figure 1b) lie in the same angular plane $\theta = const$ (Figure 2b).

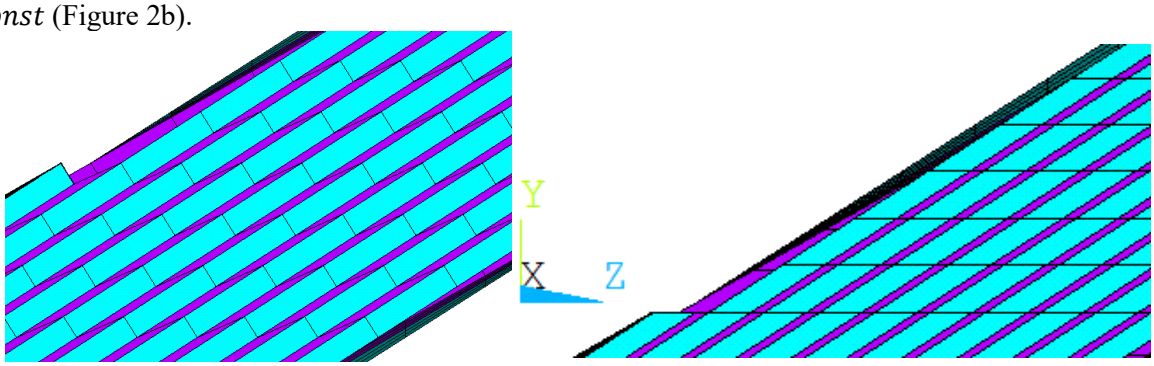

Figure 2. a) Geometry of the coil generated from Equation 1; b) Geometry generated so all nodes lie in the same $\theta = const$ plane.

In order to find the necessary values of the angle θ so all the points {A, B, D÷P} lie on the plane $\theta = \theta_k$ the following equations needed to be solved:

$$tg\theta_k = \frac{y_{ji}}{x_{ji}} \quad (6)$$

where x_{ji} and y_{ji} are the *x* and *y* coordinates of the point *j* on the *i*-th layer (Equation 4)
Inserting the components of the Equation 4 into Equation 6 gives:

$$tg\theta_k = \frac{\left(R_{\mathrm{C}i} + X_{\mathrm{r}ji}\right)\sin(\theta) + \frac{X_{\mathrm{b}ji}C(\theta)}{D(\theta)}\cos(\theta)}{\left(R_{\mathrm{C}i} + X_{\mathrm{r}ji}\right)\cos(\theta) - \frac{X_{\mathrm{b}ji}C(\theta)}{D(\theta)}\sin(\theta)} = \frac{\left(R_{\mathrm{C}i} + X_{\mathrm{r}ji}\right)\mathrm{tg}(\theta) + \frac{X_{\mathrm{b}ji}C(\theta)}{D(\theta)}}{\left(R_{\mathrm{C}i} + X_{\mathrm{r}ji}\right) - \frac{X_{\mathrm{b}ji}C(\theta)}{D(\theta)}\mathrm{tg}(\theta)} \quad (7)$$

Introducing Equation 2 and Equation 3 into Equation 7 leads to

$$tg\theta_k = \frac{\left(R_{\mathrm{C}i} + X_{\mathrm{r}ji}\right)\mathrm{tg}(\theta)\left[R_{\mathrm{C}i}^2 + \left(R_{\mathrm{C}i}\cot(\alpha_i)\cos(\theta-\theta_{0i}) + \frac{w_i}{2\pi}\right)^2\right]^{1/2} + X_{\mathrm{b}ji}\left[R_{\mathrm{C}i}\cot(\alpha_i)\cos(\theta-\theta_{0i}) + \frac{w_i}{2\pi}\right]}{\left(R_{\mathrm{C}i} + X_{\mathrm{r}ji}\right)\left[R_{\mathrm{C}i}^2 + \left(R_{\mathrm{C}i}\cot(\alpha_i)\cos(\theta-\theta_{0i}) + \frac{w_i}{2\pi}\right)^2\right]^{1/2} - X_{\mathrm{b}ji}\left[R_{\mathrm{C}i}\cot(\alpha_i)\cos(\theta-\theta_{0i}) + \frac{w_i}{2\pi}\right]\mathrm{tg}(\theta)} \quad (8)$$

Equation 8 has no close-form analytical solution. It should be noted that for the distance $X_{bji} = 0$, namely if the considered point is the center of the coil C the equation simplifies to $tg\theta_k = tg\theta$ with the obvious solution $\theta=\theta_k$. The solution algorithm was implemented in the ANSYS APDL script, and it's described in the next section.

2.1. Finding intersections of the CCT edges with the plane θ=const

The plot of the Equation 8 with for the 1st layer of the nested CCT dipole (Table 1) with the angle of intersection $\theta_k = \theta_{01}$ is shown in Figure 3. The equation is always solved in the angle range $\theta_{0i}..\theta_{0i}+360^0$, as the situation repeats for subsequent turns. The Equation 8 contains asymptotes for the denominator equal to zero:

$$\left(R_{\mathrm{C}i} + X_{\mathrm{r}ji}\right)\left[R_{\mathrm{C}i}^2 + \left(R_{\mathrm{C}i}\cot(\alpha_i)\cos(\theta-\theta_{0i}) + \frac{w_i}{2\pi}\right)^2\right]^{1/2} - X_{\mathrm{b}ji}\left[R_{\mathrm{C}i}\cot(\alpha_i)\cos(\theta-\theta_{0i}) + \frac{w_i}{2\pi}\right]\mathrm{tg}(\theta) = 0 \quad (9)$$

For $\theta_k=\pi/2+n\pi$ the tangent $tg(\theta_k)$ in Equation 8 is infinite and the corresponding solution for the angle θ was found from Equation 9. For the 3rd and 4th layer as the angle θ_0 is 270^o the equation 9 has 3 asymptotes, as shown in Figure 4. It should be noted that the solution of the Equation 8 and Equation 9 was always close to the angle θ_k. For the range of considered geometrical parameters (Table 1) the solution angle was within $\pm 0.7^o$ from the angle θ_k.

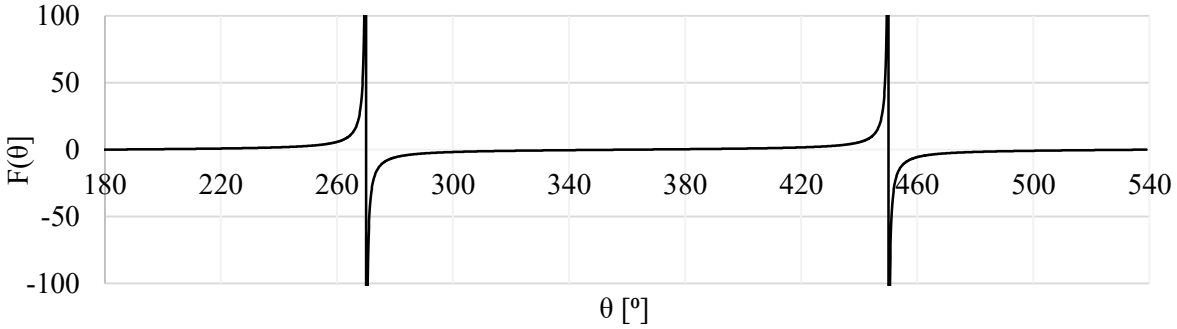

Figure 3. Equation 8 plotted for the parameters of the 1st layer (Table 1) with $\theta_k = \theta_{01}=180^0$

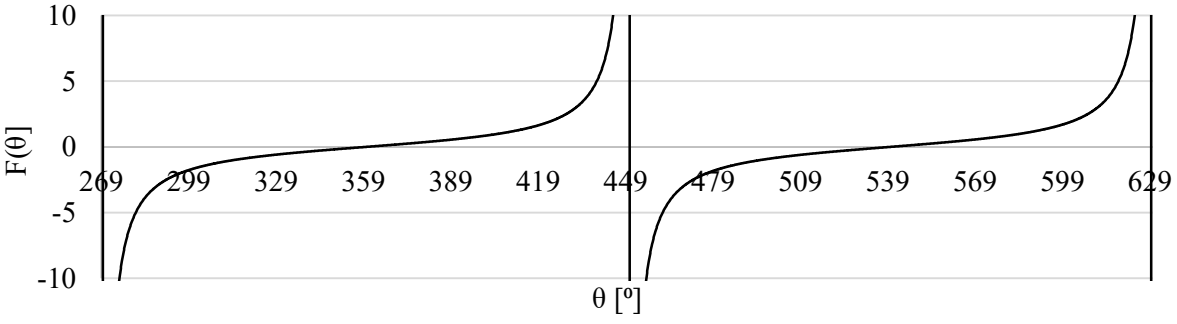

Figure 4. Equation 8 plotted for the parameters of the 3rd layer (Table 1) with $\theta_k = \theta_{03}+90^0=360^0$

The equation 8 was solved with bisection method, implemented directly in the ANSY APDL. Depending on the number of angular divisions n_θ, the equation 8 had to be solved $360 \cdot n_P/n_\theta$ times per layer. The key aspect in the solution was setting correct angle limits that capture the solution around θ_k, generally $\pm 0.7^0$ (for the given geometrical parameters), and close to the asymptotes only on one side of them. The error tolerance was set to 2e-9, for lower values convergence could not be obtained close to the asymptotes. For this error tolerance the solution required less than 30 iterations.

3. The 3D FEM model of the nested CCT dipole

The model was meshed with $n_1=n_2=n_3=3$ divisions, giving $n_P=14$ (Equation 5). The angular step was 2.8125^o (giving exactly 128 elements around the circumference), so the Equation 8 needed to be solved 14*128=1792 times per layer. Base on the computed angles the nodes were generated from Equation 1 and then the elements. First 5 turns of the 1st layer are shown in Figure 5a÷c. The end parts were generated base on the coordinates of the existing nodes (Figure 6a), 15 divisions were assumed for the end parts in the z-direction. Apart from $2n_P$ (28), 6-node wedge elements (Figure 6b) per layer, all the other elements were hexagonal in shape. The side view on the 1st layer without the interlayer insulation elements is shown in Figure 7. The full model with the outer cylinder is plotted in Figure 8a, the coils in Figure 8b, the interlayer insulation in Figure 8c, and the former channels in Figure 8d.

Solid 185 elements were used for the structure and CONTA174/TARGE170 elements for the contacts between the layers (Figure 9). The option *Initial penetration/gap* was set to *Exclude* for all the contacts. There was in total 2323088 Solid185 elements with 2594000 nodes, plus 253200 contact elements. In total 3*2594000=7.782 MDOF.

The direct generation of the meshed model, show in Figure 8, took 19 minutes. With generation of keypoints and volumes and mesh subsequent meshing the generation time was of the order of 12 hours due to the very large number of volumes ~750 000. Writing a direct script made the meshing at least 20x faster allowing more rapid model development and faster parametric runs.

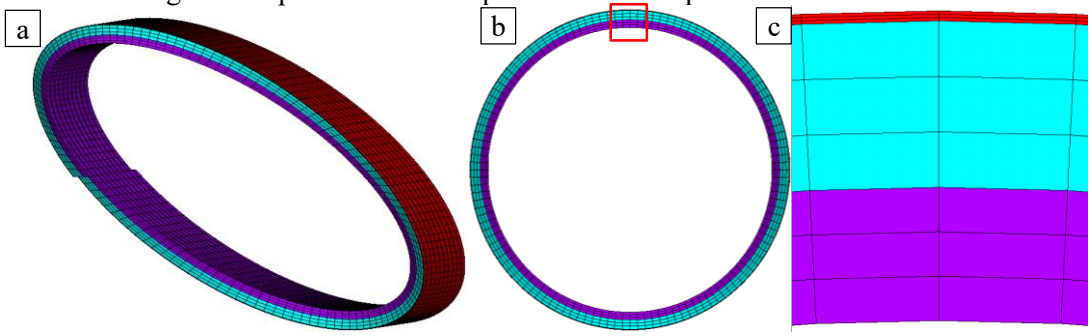

Figure 5. Mesh of 10 turns (blue – coil, violet – former, red – interlayer); a) 3D view; b) Front view (xy plane); c) Magnified view on the radial divisions.

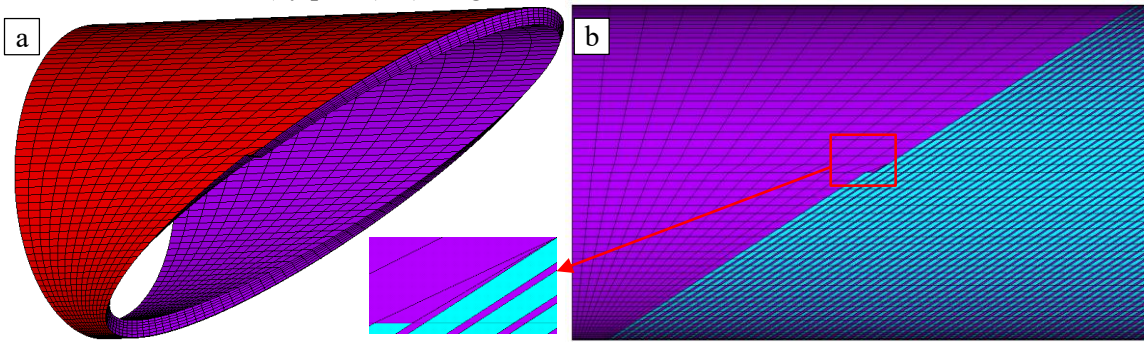

Figure 6. a) 3D view of the former end; b) Transition between the coil and the end of the former.

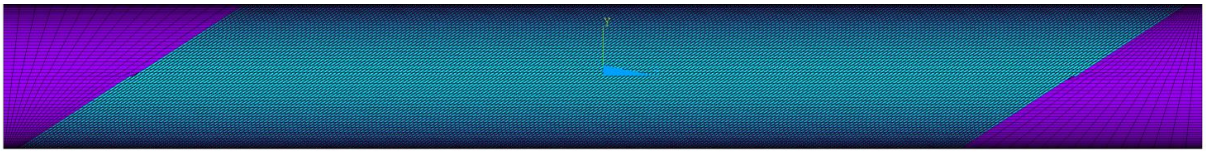

Figure 7. Side view on the 1st layer; interlayer insulation not shown.

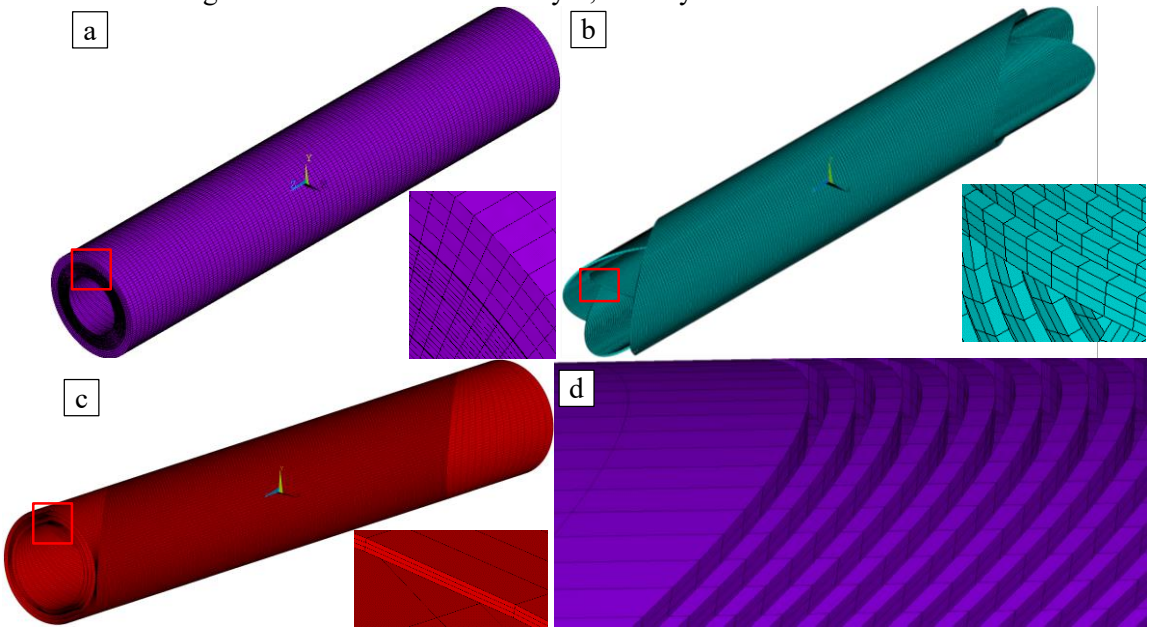

Figure 8. a) Mesh of the full model ; b) Mesh of the coils; c) The interlayer insulation; d) Detailed view of the grooves in the former.

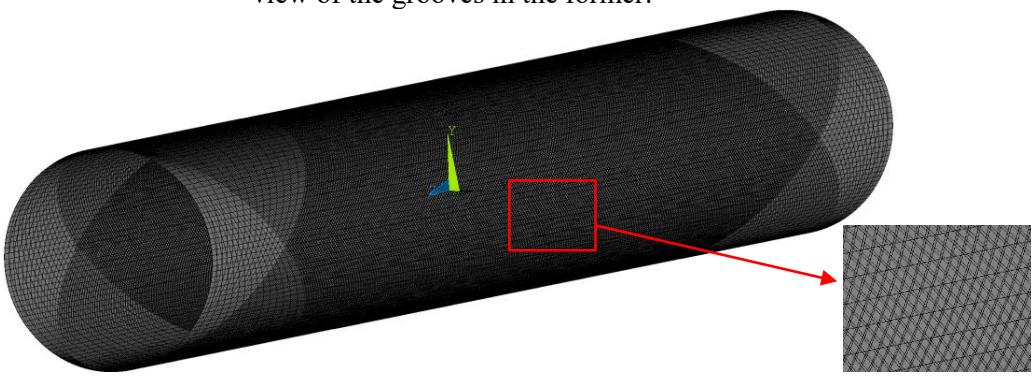

Figure 9. Contact pair between the 1st and the 2nd layer.

3.1. Material properties

Three material models were employed in the simulation. The formers and the outer cylinder were made out of high strength Aluminum 6082-T6 (Table 2) . The interlayer insulation was a composite made of Kapton and S2-glass impregnated with the CTD-101K epoxy. The interlayer composite was described with orthotropic material model with the thermal properties assuming 50 % of the S-2 glass fibers [22]. The mechanical and thermal properties of the coils (Figure 10a, b) were obtained via homogenization based on a separate 3D model (Figure 10c). Due to orthotropic properties of Nb-Ti strands plus the isotropic epoxy, the resulting properties were orthotropic as well. In order to account for the non-isotropic properties of the coils, element coordinate systems were rotated from the default Cartesian to the local frame *rbt* [18] (Figure 11).

Table 2. Material properties

Mat.	Temp. [K]	Properties
Aluminum 6082-T6	293 [20]	E=70.1 GPa, ν=0.338
	1.9 [20]	E=77.7 GPa, ν=0.327
	Thermal [19]	$\alpha_{293\text{-}1.9}$=14.2e-6
Fiberglass composite for the interlayer insulation	293 [21]	E_X=16 GPa, E_Y=30 GPa, E_Z=27 GPa, ν_{xy}=0.11, ν_{yz}=0.21, ν_{xz}=0.42, G_{XY}=5.7 GPa, G_{YZ}=6.8 GPa, G_{XZ}=4.8 GPa
	1.9 [21]	E_X=24 GPa, E_Y=37 GPa, E_Z=35 GPa, ν_{xy}=0.13, ν_{yz}=0.27, ν_{xz}=0.48, G_{XY}=9.7 GPa, G_{YZ}=11.6 GPa, G_{XZ}=8.2 GPa
	Thermal [22]	$\alpha_{x\_293\text{-}1.9}$=20.9e-6, $\alpha_{y\_293\text{-}1.9}$=$\alpha_{z\_293\text{-}1.9}$=6.8e-6
Homogenized coil [18]	293	E_X=E_Y=11.9 GPa, E_Z=59 GPa, ν_{xy}=0.36, ν_{yz}=ν_{xz}=0.07, G_{XY}=2.57 GPa, G_{YZ}=G_{XZ}=3.45 GPa (all ν defined as "PR")
	1.9	E_X=E_Y=25.8 GPa, E_Z=61.2 GPa, ν_{xy}=0.38, ν_{yz}=0.16, ν_{xz}=0.17, G_{XY}=5.7 GPa, G_{YZ}=G_{XZ}=7.27 GPa (all ν defined as are "PR")
	Thermal	$\alpha_{x\_293\text{-}1.9}$=$\alpha_{y\_293\text{-}1.9}$=23.9e-6, $\alpha_{z\_293\text{-}1.9}$=9.85e-6

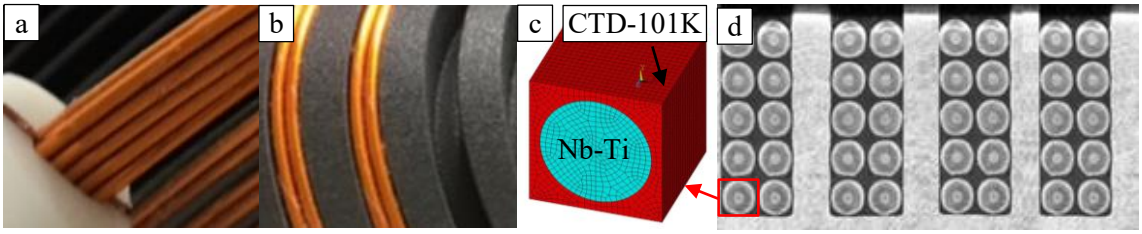

Figure 10. a) 10 Nb-Ti strand clamped for winding; b) Strands wound in the channel; c) 3D model for computing the homogenized properties of the strand with the CTD-101K resin [18]; d) Cross-section of the coil – as in the D2 orbit corrector [6].

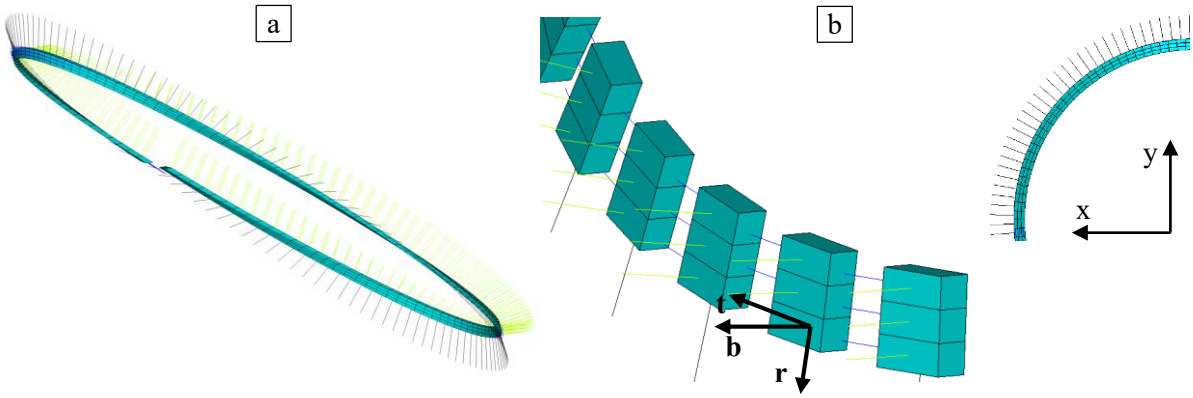

Figure 11. Element coordinate systems in the 1st turn of the 1st layer; b) Magnified view; half of the elements unselected for readability [black – r (radial), green – b (binormal), blue – t (tangent)].

3.2. Electromagnetic forces

The electromagnetic (EM) nodal force densities were mapped from the electromagnetic model (having denser mesh: 180 divisions circumferentially, 3 radially and 2 axially) to the element centroids in the mechanical model via ANSYS subroutine *MOPER,,MAP. The mapped force densities were multiplied by element volumes to obtain the forces. In order to visualize the distribution of the EM forces along one turn they were transferred to the local frame *rbt* (Figure 1) via rotation matrix (derived in [18]):

$$\begin{bmatrix} F_r \\ F_b \\ F_t \end{bmatrix} = \begin{bmatrix} cos(\theta) & sin(\theta) & 0 \\ -sin(\theta)\dfrac{C(\theta)}{D(\theta)} & cos(\theta)\dfrac{C(\theta)}{D(\theta)} & -\dfrac{R_{Ci}}{D(\theta)} \\ -sin(\theta)\dfrac{R_{Ci}}{D(\theta)} & cos(\theta)\dfrac{R_{Ci}}{D(\theta)} & \dfrac{C(\theta)}{D(\theta)} \end{bmatrix} \begin{bmatrix} F_x \\ F_y \\ F_z \end{bmatrix} \quad (10)$$

where $C(\theta)$ and $D(\theta)$ are given by Equation 2 and Equation 3

The distribution of the radial force is shown in Figure 12a. With maximum positive values near the angle θ=45° for the layers 1 and 2 and maximum negative values for the angle θ=135°. The radial force was responsible for the oval shape of the magnet during powering (Figure 15). The binormal force (Figure 12b) was the largest out of F_r and F_t, whereas F_t the smallest (Figure 12c). The values of the forces F_r, F_b, F_t over the turns 100÷101 are plotted in Figure 13. The same values of forces were repeating along the entire straight section of the magnet. Forces in the ends were smaller due to lower magnetic field there. The period of variation of the force F_b was twice smaller compared to the forces F_r and F_t. Close to sinusoidal shape was observed for the forces F_r and F_t, whereas for the binormal force F_b considerable deviation from sine-like shape occurred.

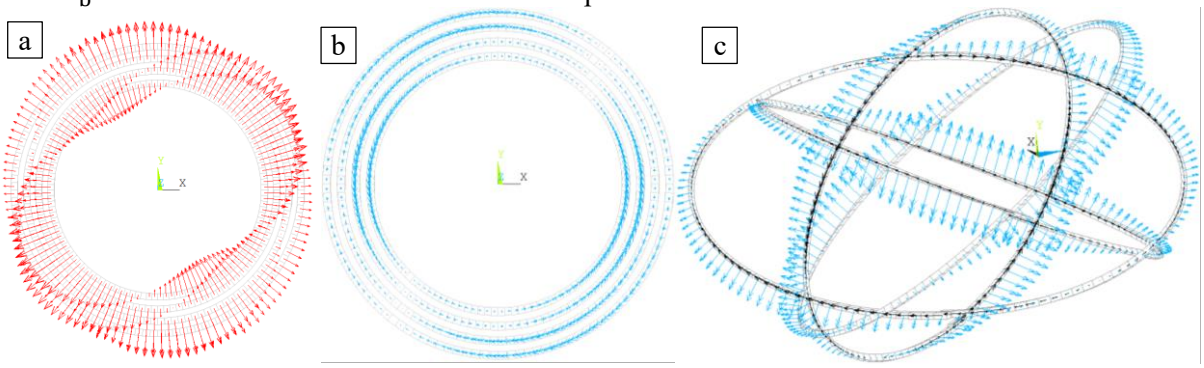

Figure 12. Electromagnetic forces acting on the 100th turn of each of the layers (coil meshed with 1 element radially and 120 circumferentially); a) Force F_r; b) Force F_b; c) Forces F_b and F_t in 3D.

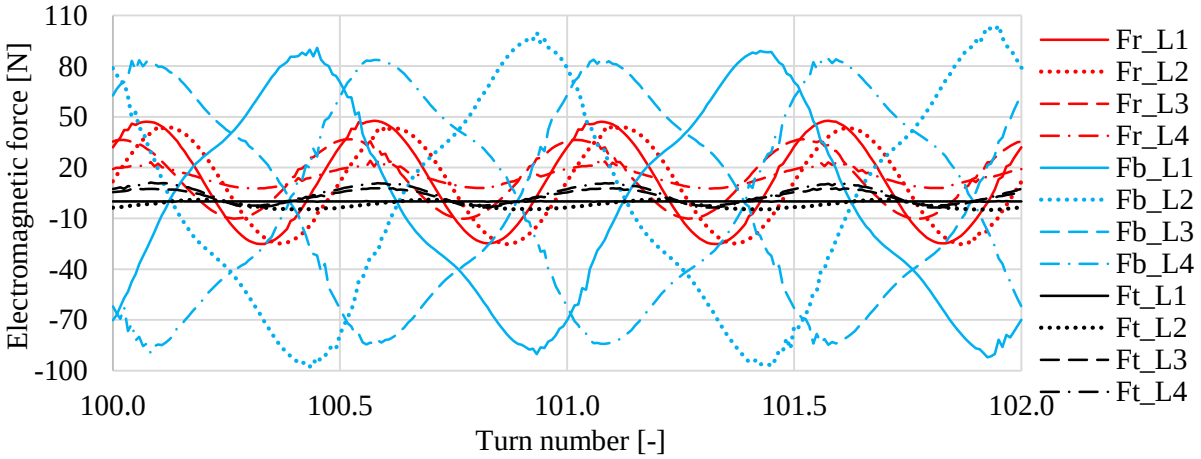

Figure 13. Electromagnetic forces along the 100÷101 turns for all 4 layers.

3.3. Boundary conditions

Two types of boundary conditions (BCs) were considered in the simulations. Corresponding to the 1st and the 2nd design iterations of the nested CCT dipole (Figure 14). The outer cylinder has 4 grooves into where flat bars (keys) are fitted with interference. The keys are in turn connected with the grooves of

the yoke (Figure 14b). The clearance of the yoke grooves is large enough, so the more contracting Aluminum cylinder can shrink independently from the yoke (smaller α_T) in the axial and radial directions. In order to model such boundary condition the displacement of the node corresponding to the center of the keys was blocked in the circumferential direction along the whole length of the cylinder (Figure 14). The top surface of the cylinder was fully constrained in the z-direction, to represent the test in a vertical cryostat.

The castellations in the formers, visible in Figure 14 were not included in the geometry in this study. Here, we wanted to check if the structure can satisfy the design constraints only relying on bonding between the layers. The key issue was checking if the maximum shear stresses in the interlayer insulation were below the assumed design limit of 10 MPa. The answers are given in the next section.

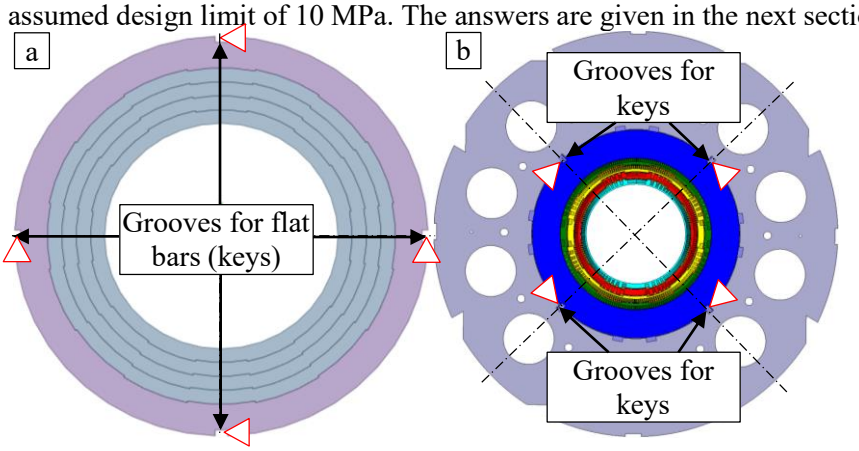

Figure 14. a) First design of the nested CCT dipole, only coils and the outer cylinder; b) 2nd iteration of the design, coils, outer cylinder and the yoke; boundary conditions indicated by triangles.

4. Results of the simulations for the nested CCT dipole

Direct solver was used for the solution with the Distributed Memory Parallel mode. The model required ~550 GB of RAM memory. As the system was limited to 192 GB, the computation run in the out of core mode on fast SSD M.2 PCIe discs.

The analysis consisted of 2 steps: cool-down from 293 K to 1.9 K and loading with EM forces. The results related to EM forces only were obtained in post-processing by subtracting the results of the 1st load step from the results of the 2nd load step. The 1st step required 5 iterations of the Direct Solver (factorizations) and the 2nd step six, with the average amount of written data to SSD discs of ~3.5 TB per iteration. Giving ~38.5 TB for the entire simulation, so an important number for considerations of SSD wear. Solution time was ~24 hours (with 16x3.5 GHz cores).

The maximum total deformation due to EM forces only for the diagonal BCs (as in Figure 14b) was 161 µm (Figure 15), so considerably more than for the case with symmetric BCs (as in Figure 14a) with 92.3 µm (Figure 16). For the field quality reasons, the deformation of the coils should be ideally below 50 µm. The symmetric BCs are therefore beneficial in lowering the deformations due to EM forces.

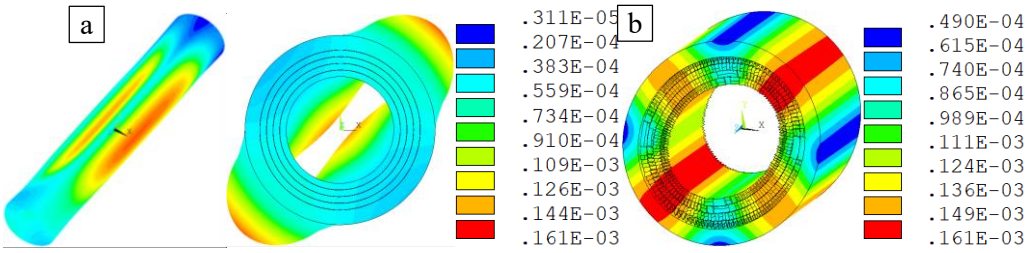

Figure 15. Deformations (unit m) due to EM forces only for the model with diagonal BCs (Figure 14b); a) the whole magnet; b) Middle part only z=-50-50 mm.

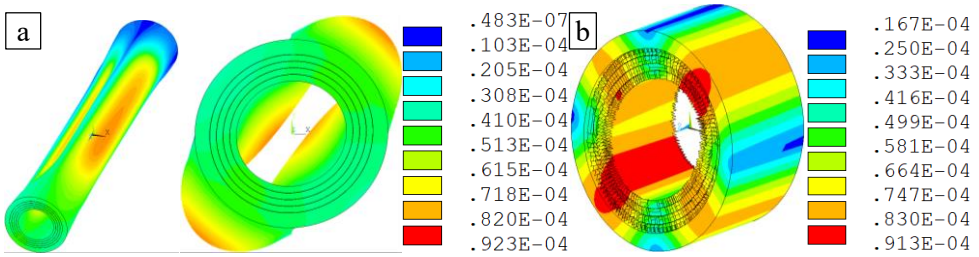

Figure 16. Deformations (unit m) due to EM forces only for the model with symmetric BCs (Figure 14a); a) the whole magnet; b) Middle part only z=-50-50 mm.

The maximum deformation due to EM forces only for the symmetric BCs did not lie in the center of the magnet, but rather was shifter towards the free end (Fig. 16), an effect not observed for the diagonal BCs.

The shear stresses in the interlayer composite for the model with diagonal BCs are shown in Figure 17 and **Błąd! Nie można odnaleźć źródła odwołania.**. The maximum value after cool-down was 32.7 MPa and 35.4 MPa after powering, whereas due to EM forces only 11.8 MPa. These results clearly showed that the thermal stresses were 3x larger than Lorentz force induced stresses, so actually the layers would debond already due to the cool-down to 1.9 K. For the symmetric BCs, maximum shear stresses due to cool-down were slightly smaller: after cool-down 32.7 MPa (Figure 19), after powering 34.2 MPa and due to powering 8.0 MPa (Figure 20).

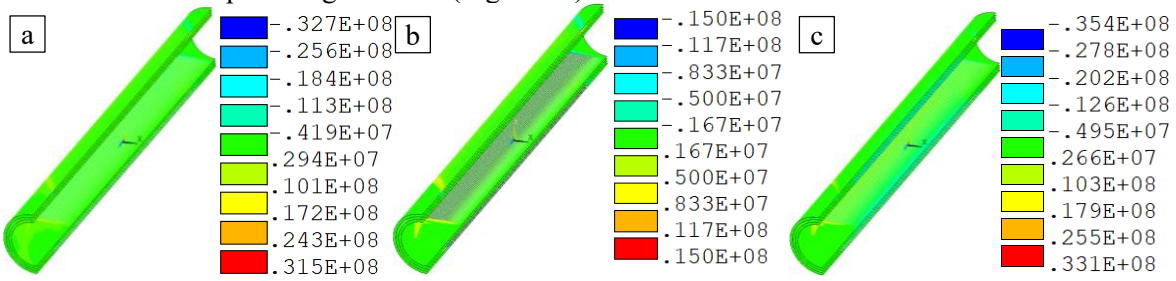

Figure 17. Shears stresses (in Pa) in the interlayer composite, diagonal BCs (Figure 14b); a) After cool-down to 1.9 K; b) After cool-down to 1.9 K with values limited to ±15 MPa; c) After powering.

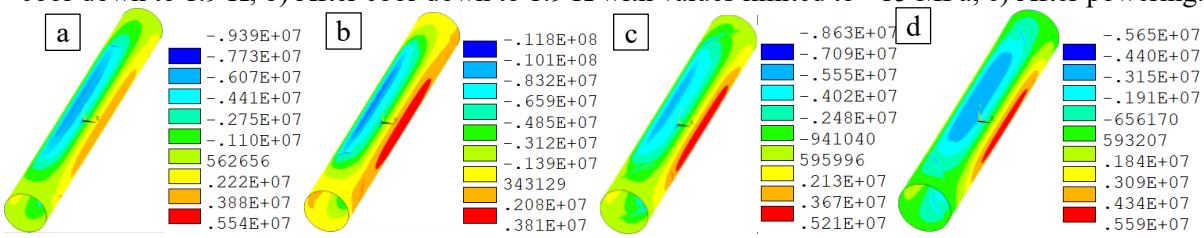

Figure 18. Shears stresses (in Pa) in the interlayer composite for the model with diagonal BCs due to EM forces only; a) Layer 1; b) Layer 2; c) Layer 3; d) Layer 4

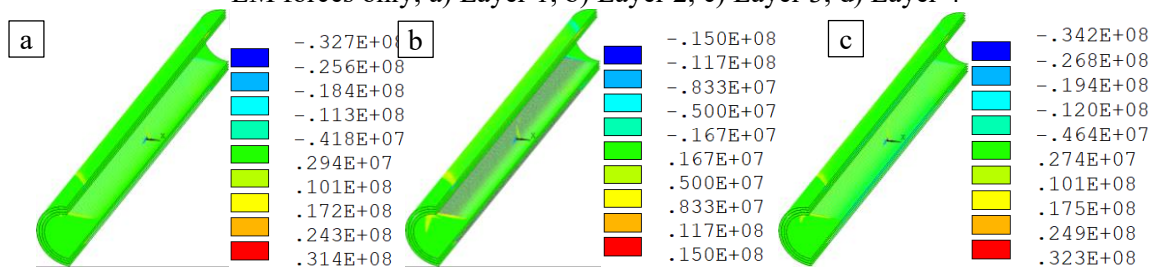

Figure 19. Shears stresses (in Pa) in the interlayer composite, symmetric BCs (Figure 14a); a) After cool-down to 1.9 K; b) After cool-down to 1.9 K with values limited to ±15 MPa; c) After powering.

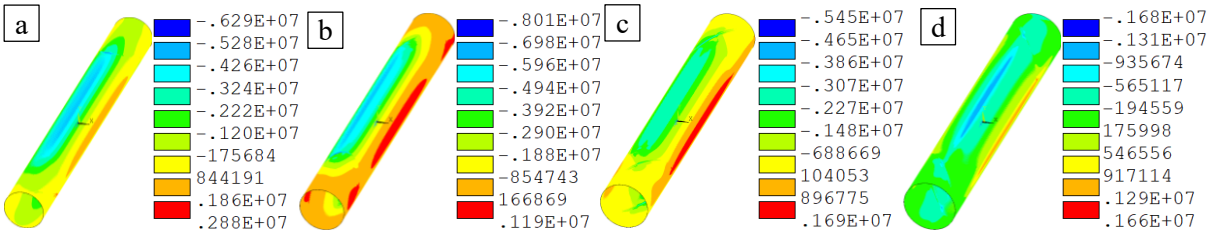

Figure 20. Shears stresses (in Pa) in the interlayer composite due to EM forces only, symmetric BCs; a) Layer 1; b) Layer 2; c) Layer 3; d) Layer 4.

The maximum shear stress in the coil (homogenized strands with resin) for the diagonal BCs and for the cable frame τ_{rb} was 12.3 MPa for the 1st step, 13.6 MPa for the 2nd step and 6.9 MPa for the 3rd step (EM forces only). Analogous values for τ_{bt} were 6.3 MPa, 6.2 MPa and 4.6 MPa and for τ_{rt} 4.8 MPa, 4.3 MPa and 3.4 MPa. For the symmetric BCs these shear stresses were smaller: τ_{rb}: 12.3 MPa, 12.8 MPa, 4.2 MPa; τ_{bt} 4.0 MPa, 4.4 MPa, 2.8 MPa and τ_{rt} 2.8 MPa, 3.5 MPa and 2.4 MPa. All shear stresses caused by powering only were below 7.0 MPa, for both boundary condition types, indicating that the debonding from the Aluminum formers is not likely to occur during powering - assuming that the shear limit of 10 MPa holds. The occurrence of debonding is of a large importance as it could become a source of a, very undesirable, training in the magnet. The compressive stresses in the interlayer insulation were low w.r.t. the compressive limit of 1360 MPa at 4 K [22], with maximum value in the radial direction for the symmetric BCs during powering (2nd step) of 48 MPa, in the circumferential direction of 156 MPa (local effect) and 162 MPa in the axial direction.

5. Conclusions

The analysis of the 3D model confirmed the necessity of including castellations in the design, as shear stresses were much above the shear strength limit of 10 MPa. The maximum shear stress $\tau_{r\varphi}$, after cool-down to 1.9 K, was 32.7 MPa for both diagonal and symmetric boundary conditions, whereas the maximum shear stress due to electromagnetic forces only was 11.8 MPa and 8.0 MPa respectively. So the maximum shear stresses caused by temperature were 2.8 and 4.1 times larger than stresses caused by the Lorentz forces. Large thermal stresses are caused by the incompatibility of the coefficients of thermal contraction between the Aluminum (formers) - $\alpha_{293\text{-}1.9}$=14.2e-6 and the fiberglass impregnated with CTD-101K resin - $\alpha_{x\_293\text{-}1.9}$=20.9e-6 (through thickness). In the simulation the volume fraction of the resin in the interlayer composite was assumed as 50 %, if the content of S-2 glass fibers would be larger the thermal contraction coefficient would decrease. However, increasing the fiberglass content can be difficult, as it can hinder the resin flow during impregnation. Therefore, the assumption of 50 % content of fiberglass looks realistic. Another possibility of decreasing the thermal stresses in the interlayer would result from employing other type of epoxy resin with lower coefficient of thermal contraction. However, this would require extensive R&D work in verifying the mechanical behavior of such a resin and its performance with complex coils – such as for the nested CCT dipole.

The symmetric boundary conditions show considerably smaller deformations of the coils - 92.3 μm versus 161 μm, as well as smaller shear stresses, therefore they should be considered in the final design due to field quality reasons. The FEM modeling of the castellated nested CCT dipole will be the subject of the subsequent work.

References

[1] Meyer DI and Flasck R 1970 A new configuration for a dipole magnet for use in high energy physics applications *Nuclear Instruments and Methods* **80(2)** p 339-41
[2] Brouwer LN 2016 *Canted-cosine-theta superconducting accelerator magnets for high energy physics and ion beam cancer therapy* **36** (EuCARD-2 Scientific Monograph)
[3] Caspi S et al. 2015 Test results of CCT1—A 2.4 T Canted-Cosine-Theta dipole magnet *IEEE T APPL SUPERCON* **25(3)** 4002304

[4] Prestemon S 2018 Status update from LBNL MDP - FCC - EuroCirCol Meeting 03/12/2018. MDP-FCC-EuroCirCol coordination meeting 06 https://indico.cern.ch/event/776591/
[5] Apollinari G, Béjar AI, Brüning O, Fessia P, Lamont M, Rossi L and Tavian L 2017 *High-Luminosity Large Hadron Collider (HL-LHC). Technical Design Report V. 0.1* (CERN Yellow Reports: Monographs Geneva: CERN) http://dx.doi.org/10.23731/CYRM-2017-004
[6] Kirby G et al. 2018 Hi-Lumi LHC twin aperture orbit correctors 0.5-m model magnet development and cold test *IEEE T APPL SUPERCON* **28(3)** 4002205
[7] Mangiarotti FJ et al. 2019 Test of short model and prototype of the HL-LHC D2 orbit corrector based on CCT technology *IEEE T APPL SUPERCON* **29(5)** 4002305
[8] Anferov V 2005 Combined X-Y scanning magnet for conformal proton radiation therapy *Medical Physics* **32(3)** p 815-8
[9] Montenero G, Auchmann B, Brouwer L, Calzolaio C, Caspi S, Rolando G and Sanfilippo S 2018 Mechanical structure for the PSI Canted-Cosine-Theta (CCT) magnet program *IEEE T APPL SUPERCON* **28(3)** 4002805
[10] Montenero G et al. 2019 Coil manufacturing process of the first 1-m-long Canted–Cosine–Theta (CCT) model magnet at PSI *IEEE T APPL SUPERCON* **29(5)** 4002906
[11] Wang X, Caspi S, Dietderich DR, Ghiorso WB, Gourlay SA, Higley HC, Lin A, Prestemon SO, van der Laan D and Weiss JD 2018 A viable dipole magnet concept with REBCO CORC® wires and further development needs for high-field magnet applications. *Supercond. Sci. Technol.* **31** 045007
[12] Brouwer L, Caspi S and Prestemon S 2015 Structural analysis of an 18 T hybrid Canted–Cosine–Theta superconducting dipole *IEEE T APPL SUPERCON* **25(3)** 4000404
[13] Brouwer L, Arbelaez D, Caspi S, Felice H, Prestemon S and Rochepault E 2014 Structural design and analysis of Canted–Cosine–Theta dipoles *IEEE T APPL SUPERCON* **24(3)** 4001506
[14] Caspi S, Arbelaez D, Brouwer L, Gourlay S, Prestemon S and Auchmann B 2017 Design of a Canted-Cosine-Theta superconducting dipole magnet for future colliders *IEEE T APPL SUPERCON* **27(4)** 4001505
[15] Caspi S et al. 2015 Design of an 18-T Canted Cosine–Theta superconducting dipole magnet *IEEE T APPL SUPERCON* **25(3)** 4000205
[16] Auchmann B, Brouwer L, Caspi S, Gao J, Montenero G, Negrazus M, Rolando G and Sanfilippo S 2018 Electromechanical design of a 16-T CCT twin-aperture dipole for FCC *IEEE T APPL SUPERCON* **28(3)** 4000705
[17] Brouwer L, Arbelaez D, Caspi S, Marchevsky M and Prestemon S 2018 Improved modeling of Canted–Cosine–Theta magnets *IEEE T APPL SUPERCON* **28(3)** 4001006
[18] Ortwein R, Wachal P, Blocki J, Kirby G and van Nugteren J 2020 FEM modelling of multilayer Canted-Cosine-Theta (CCT) magnets with orthotropic material properties *Cryogenics* https://doi.org/10.1016/j.cryogenics.2020.103041
[19] Ventura G and Perfetti M 2014 *Thermal properties of solids at room and cryogenic temperatures* (Dordrecht, Heidelberg, New York, London: Springer)
[20] Ekin JW 2006 *Experimental techniques for low-temperature measurements. Cryostat design, material properties, and superconductor critical-current testing* (New York: Oxford University Press)
[21] Reed RP, Fabian PE and Bauer-McDaniel TS 1996 Elastic properties of composite Iter insulation systems: Advances in Cryogenic Engineering Materials vol 42 ed Summers LT (Boston: Springer)
[22] CTD-101K Epoxy Resin System [accessed 30 August 2019] https://ncsx.pppl.gov/NCSX_Engineering/Materials/InsulationProperties/CTD-101K_Datasheet_2003.pdf